Bergische Universität Wuppertal

Fakultät für Mathematik und Naturwissenschaften

Institute of Mathematical Modelling, Analysis and Computational Mathematics (IMACM)

Preprint BUW-IMACM 25/07

Sergey Pereselkov, Venedikt Kuz'kin, Matthias Ehrhardt, Sergey Tkachenko, Alexey Pereselkov and Nikolay Ladykin

Holographic Reconstruction in the Presence of Intense Internal Waves Traveling Along an Acoustic Path

June 22, 2025

http://www.imacm.uni-wuppertal.de

Article

Holographic Reconstruction in the Presence of Intense Internal Waves Traveling Along an Acoustic Path

Sergey Pereselkov [1,*], Venedikt Kuz'kin [2], Matthias Ehrhardt [3], Sergey Tkachenko [1], Alexey Pereselkov [1] and Nikolay Ladykin [1]

[1] Voronezh State University, Mathematical Physics and Information Technology Department , 394018 Voronezh, Russia; tkachenko.edu@yandex.ru (S.T.); pereselkov.edu@yandex.ru (A.P.); ladykin.edu@yandex.ru (N.L.)
[2] Prokhorov General Physics Institute of the Russian Academy of Sciences, 119991, Moscow, Russia ; kumiov@yandex.ru
[3] University of Wuppertal, Chair of Applied and Computational Mathematics, Gaußstraße 20, 42119 Wuppertal, Germany; ehrhardt@uni-wuppertal.de
* Correspondence: pereselkov@yandex.ru

Abstract: This paper explores how intense internal waves affect the holographic reconstruction of the sound field from a moving source in shallow water. It is assumed that these waves propagate along the acoustic path between the source and receiver. This introduces inhomogeneities into the waveguide, causing significant coupling between acoustic modes. The work analyzes the effect of these traveling internal waves on the structure of the interferogram and resulting hologram of the moving source. This study is based on numerical simulations that consider mode coupling induced by internal wave activity. Within this framework, the interferogram (the received sound intensity distribution in the frequency-time domain) and the hologram (the two-dimensional Fourier transform of the interferogram) of a moving source are examined in the presence of space-time inhomogeneities caused by intense internal waves. A key finding is that under the influence of internal waves, the hologram is divided into two regions corresponding to the unperturbed and perturbed components of the sound field. This structure allows for the extraction and reconstruction of the interferogram corresponding to the unperturbed field as it would appear in a shallow water waveguide without internal waves. The paper provides an estimate of the reconstruction error associated with this approach.

Keywords: internal waves; interferogram; hologram; horizontal refraction; shallow water

---

1. Introduction

In recent years, there has been a growing interest among scientists in applying *interferometric signal processing* (ISP) techniques to the field of underwater acoustics. ISP relies on the stable characteristics of interference patterns produced by broadband acoustic fields in shallow water waveguides [1,2]. For a comprehensive overview of ISP methodologies, readers are directed to key foundational studies such as [3–5]. Several studies have applied ISP to various practical tasks. For instance, in works [6,7], ISP techniques are used to estimate waveguide-invariant parameters. The study [8] demonstrates how ISP can be applied to weak signals, with signal enhancement achieved through array beamforming. In [9], ISP is used for seabed classification based on acoustic signals generated by passing vessels. A method for estimating the range to a source in shallow water using ISP is proposed in [10]. A range-independent invariant estimation approach based on ISP is explored in [11]. Furthermore, [12] applies ISP to interpret interference fringes in terms of eigenray (or eigenbeam) arrival times. Finally, ISP has been adapted for deep-sea passive sonar applications in [13,14], demonstrating its versatility across different underwater acoustic environments.

One of the most promising approaches in interferometric signal processing (ISP) is known as *holographic signal processing* (HSP) [15,16]. The fundamental physical and mathematical principles of hologram generation were first presented in [15]. Within the HSP framework, a quasi-coherent integration of sound intensity in the frequency-time domain results in the formation of an *interferogram*

$I(\omega, t)$ [16]. To analyze the accumulated intensity distribution, a two-dimensional Fourier transform (2D-FT) is applied to $I(\omega, t)$. The resulting transform is referred to as the *Fourier hologram*, or simply the hologram, and is denoted as $F(\tau, \widetilde{\nu}) = \mathcal{F}_{2D}\{I(\omega, t)\}$. The hologram $F(\tau, \widetilde{\nu})$ concentrates the acoustic energy represented in $I(\omega, t)$ into localized focal regions that arise due to the interference of different modes.

During the initial development of HSP, it was assumed that waveguide parameters remained constant in space and time. However, acoustic signal propagation in practical scenarios often occurs in waveguides affected by hydrodynamic disturbances. The application of HSP to a stationary source under real-world conditions was first explored experimentally in [17]. The study demonstrated that hydrodynamic perturbations of the waveguide distort the interferogram $I(\omega, t)$ and enlarge the focal regions in the resulting hologram $F(\tau, \widetilde{\nu})$. In the presence of inhomogeneities, the hologram $F(\tau, \widetilde{\nu})$ can be represented as a superposition of two components: one corresponding to the unperturbed waveguide, and one arising from the perturbations. This two-component structure was used in [17] to interpret experimental data from the SWARM'95 experiment [18,19]. The observed waveguide inhomogeneities during the SWARM'95 experiment were primarily caused by *intense internal waves* (IIWs) [19–22], a widespread hydrodynamic phenomenon in the ocean [20–22]. In the SWARM'95 experiment, two acoustic paths were used, which were formed by a single source and two spatially separated vertical receiving arrays. The first acoustic path was oriented at a small angle to the wavefront of IIWs. The presence of IIWs structures induces a pronounced horizontal refraction of the acoustic rays. In our previous paper [24], we analyzed the variations in the hologram structure of a moving source in cases of significant horizontal refraction of sound rays due to IIWs. In the SWARM'95 experiment, the second acoustic path was oriented across the wavefront of the IIWs. With this orientation, the IIWs propagated along the acoustic path between the source and receiver. In this case, the IIWs did not cause horizontal refraction, but rather led to significant scattering of sound energy between acoustic modes. In other words, they induced mode coupling. This phenomenon was not considered in our previous paper [25]. However, understanding the features of hologram structure variations caused by significant mode coupling due to IIWs is crucial for developing HSP. Therefore, the current paper is dedicated to analyzing this phenomenon.

This paper aims to study the influence of intense internal waves (IIWs) on holographic reconstruction of a moving source sound field in shallow water in the presence of IIWs traveling along the acoustic path between the source and receiver, which cause significant coupling between acoustic modes. This study is based on numerical simulations that consider mode coupling induced by internal wave activity. Within this framework, we examine the interferogram (the received sound intensity distribution in the frequency-time domain) and the hologram (2D-FT of the interferogram) of moving sources in the presence of space-time inhomogeneities caused by intense internal waves. One of the paper's key findings is that under the influence of internal waves, the hologram is divided into two distinct regions corresponding to the unperturbed and perturbed components of the sound field, respectively. This structure allows us to extract and reconstruct the interferogram corresponding to the unperturbed field as it would appear in a shallow water waveguide without internal waves. The paper also provides an estimate of the reconstruction error associated with this approach.

Our research relies on numerical simulations of sound field propagation in three-dimensional (3D) inhomogeneous shallow water waveguides. The structure of the sound field can be significantly affected by 3D inhomogeneities in the propagation medium due to sound scattering by IIWs. Modeling broadband, low-frequency sound fields in these 3D environments requires significant computational resources and often necessitates advanced numerical methods and high-performance computing platforms to ensure physically realistic results. There are five principal groups of numerical approaches for simulating sound field propagation in inhomogeneous shallow water waveguides [25]: 3D Helmholtz Equation (3DHE) models [26–28]; 3D Parabolic Equation (3DPE) models [29–35]; 3D Ray-based (3DR) models [36,37,52]; Vertical Modes and 2D Modal Parabolic Equation (VMMPE) models [23,24,38–40]; Vertical Coupled Modes with Horizontal Rays (VCMHR) models [41–50].

Our research focuses on the low-frequency sound field within two frequency bands: 100–120 Hz and 300–320 Hz. We assume that the spatial inhomogeneities of the shallow water waveguide are generated by internal wave-induced (IIW) inhomogeneities propagating along the acoustic path between the source and receiver. These inhomogeneities, induced by IIWs, lead to strong scattering effects. Of the five modeling approaches mentioned, the VCMHR model is the most suitable for our scenario. It is well-adapted to low-frequency sound propagation in a shallow water waveguide with IIWs. The VCMHR model accurately incorporates boundary conditions and captures the essential physics of vertical mode coupling due to environmental variability. In contrast, 3D models are generally better suited to high-frequency scenarios and fail to adequately describe mode coupling at low frequencies in shallow water. Although the 3DHE and 3DPE methods provide high-fidelity solutions, they are computationally prohibitive in this context due to the complexity of the 3D problem. VMMPE models, on the other hand, effectively handle horizontal refraction but lack sufficient capability for mode coupling, a key process in our paper. Therefore, we selected the VCMHR framework as the most appropriate numerical tool for simulating sound field propagation under the influence of IIWs.

This paper is organized into six sections. After the introduction in Section 1, Section 2 describes the 3D model of a shallow water waveguide in the presence of IIWs traveling along an acoustic path. Next, in Section 3, we derive the mathematical model of the interferogram $I(\omega, t)$ and, in Section 4, the hologram $F(\tau, \widetilde{\nu})$ of a moving source in a shallow water waveguide with significant mode coupling caused by IIWs. We develop an algorithm for the numerical calculation of the interferogram and hologram of a moving source. It is based on a set of differential equations for the mode amplitudes. This algorithm takes into account the mode coupling caused by IIWs propagating along the acoustic path between the source and receiver. In Section 5, we analyze the results of the numerical modeling of the interferogram $I(\omega, t)$ and hologram $F(\tau, \widetilde{\nu})$ of a broadband sound source in a shallow water waveguide in the presence of IIWs causing significant mode coupling. The numerical modeling considers the influence of IIWs on the interferogram $I(\omega, t)$ and hologram $F(\tau, \widetilde{\nu})$ of the source sound field for two cases of source parameters. The first case involves a stationary acoustic path between the source and receiver (non-moving source). The second case involves a non-stationary acoustic path (i.e., a moving source). To compare the numerical modeling results for both cases in the presence of IIWs, the initial data for the simulations are chosen to be the same. The influence of IIWs on holographic reconstruction error is analyzed. The results are summarized in Section 6 of the paper.

2. Waveguide Model in the Presence of IIWs

The waveguide model in IIWs propagating along the acoustic path is presented in Section 2, which consists of two parts. The first part, Section 2.1, describes the shallow water waveguide model with inhomogeneities due to IIWs. Section 2.2 examines the model of IIWs and its parameters.

2.1. Waveguide Model with Inhomogeneities due to IIWs

In this section, we present the three-dimensional model of the shallow water waveguide used in our study (see Figure 1). The waveguide is defined in a Cartesian coordinate system (X, Y, Z) and modeled as a water layer with spatially and temporally varying sound speed $c(\mathbf{r}, z, t)$ and density $\rho(\mathbf{r}, z, t)$. Here, $\mathbf{r} = (x, y)$ denotes the horizontal position vector. The water column is bounded above by the free surface at $z = 0$ and below by the sea bottom at $z = H$.

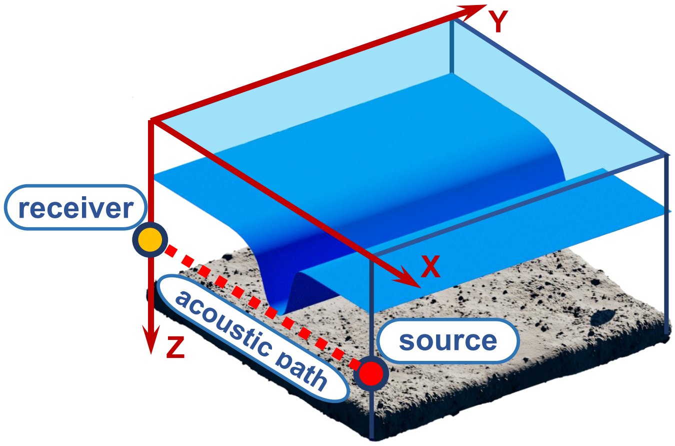

Figure 1. Model of shallow water in the presence of an IIWs traveling along an acoustic path between source and receiver.

The density and refractive index of the seabed are given by ρ_b and $n_b(1+\mathrm{i}\varkappa)$, respectively [51,52], where $\varkappa$ is the attenuation factor, defined as $\varkappa = \chi c_b/(54.6f)$. In this expression, χ represents the bottom loss coefficient. c_b is the acoustic velocity in the bottom layer, and f is the sound frequency.

The spatiotemporal variation of the sound speed within the water column can be expressed as

$$c(\mathbf{r}, z, t) = \bar{c}(z) + \tilde{c}(\mathbf{r}, z, t), \tag{1}$$

where $\bar{c}(z)$ is the background sound speed profile in the absence of internal wave activity, and $\tilde{c}(\mathbf{r}, z, t)$ accounts for the perturbations induced by internal inertia waves (IIWs).

Based on Eq. (1), the squared refractive index in the water column is given by

$$n^2(\mathbf{r}, z, t) = \bar{n}^2(z) + \tilde{n}^2(\mathbf{r}, z, t), \tag{2}$$

where $\bar{n}^2(z)$ is the unperturbed refractive index profile, and $\tilde{n}^2(\mathbf{r}, z, t)$ is the fluctuation component caused by IIWs. Following the formulation in [22,23], the perturbation term can be described as

$$\tilde{n}^2(\mathbf{r}, z, t) = -2QN^2(z)\,\zeta(\mathbf{r}, z, t), \tag{3}$$

where $Q \approx 2.4\ \mathrm{s}^2/\mathrm{m}$ is a water-specific physical constant, $N(z) = \left(-\frac{g}{\rho}\frac{d\rho}{dz}\right)^{1/2}$ is the buoyancy frequency, and $\zeta(\mathbf{r}, z, t)$ denotes the vertical displacements within the water column induced by IIWs.

2.2. IIWs Parameters

In this section, we present a space-time model of IIWs $\zeta(\mathbf{r}, z, t)$ and their parameters. According to the predominance of the first gravity mode [20–22], vertical displacements within the water column induced by IIWs can be expressed as follows:

$$\zeta(\mathbf{r}, z, t) = \Phi_1(z)\,\zeta_0(\mathbf{r}, t), \tag{4}$$

where $\Phi_1(z)$ denotes the eigenfunction of the first gravity mode, normalized at depth z_0: $\Phi_1(z_0) = 1$. According to [20–22], the gravity modes $\Phi_n(z)$ and their corresponding dispersion characteristics $\Omega_n(K)$ represent the eigenfunctions and eigenvalues of the following Sturm–Liouville problem:

$$\frac{d^2\Phi_n(z)}{dz^2} + \left(\frac{N^2(z)}{\Omega_n^2(K)} - 1\right)K^2\Phi_n(z) = 0, \qquad \Phi_n(0) = \Phi_n(H) = 0. \tag{5}$$

The gravity modes $\Phi_n(z)$ satisfy the following normalization condition [20–22]:

$$\int_0^H N^2(z)\Phi_n(z)\Phi_m(z)\,dz = \delta_{nm}, \tag{6}$$

where δ_{nm} is the Kronecker delta. For typical stratifications on the continental shelf, the function $\Phi(z)$ depends weakly on the frequency and the wave number. In the Eq. (4) $\zeta(\mathbf{r}, z, t) = \zeta_0(x, y, t)$ are the vertical displacements in the waveguide water layer due to IIWs at a depth z_0 in the thermocline water layer.

According to [20–22] we can represent IIWs as a sequence of internal solitons (IS), which are soliton-like solutions of the Korteweg-de Vries (KdV) equation:

$$\frac{\partial \zeta_0}{\partial t} + u\frac{\partial \zeta_0}{\partial x} + a\zeta_0\frac{\partial \zeta_0}{\partial x} + b\frac{\partial^3 \zeta_0}{\partial x^3} = 0. \tag{7}$$

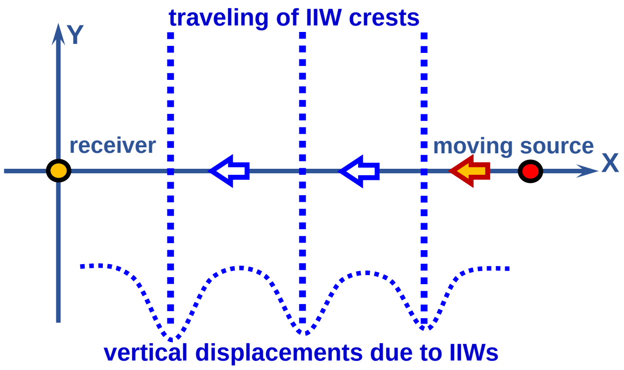

Figure 2. Shallow water waveguide geometry in horizontal plane (x, y). Acoustic path between a moving source and a nonmoving receiver. Traveling of IIWs direction.

The parameters of Eq. (7) are determined by the stratification of the water layer:

$$a = \frac{3u}{2}\int_0^H \left(\frac{d\Phi}{dz}\right)^3 dz \Big/ \int_0^H \left(\frac{d\Phi}{dz}\right)^2 dz, \tag{8}$$

$$b = \frac{u}{2}\int_0^H \Phi^2 dz \Big/ \int_0^H \left(\frac{d\Phi}{dz}\right)^2 dz, \qquad u = \frac{\Omega(K)}{K} \tag{9}$$

Given the selected geometry of the problem (see Figure 2), the vertical displacement $\zeta_0(\mathbf{r}, t)$ in the water layer of the waveguide can be represented as follows:

$$\zeta_0(\mathbf{r}, t) = \sum_{n=1}^{N} B_n \operatorname{sech}^2\left[\frac{x - D_n - u_n t}{\eta_n}\right], \tag{10}$$

where N denotes the number of internal solitons (IS) in the train, B_n is the amplitude of the n-th soliton, u_n is the propagation speed, D_n is the initial horizontal displacement, and η_n is the width of the soliton.

IIWs are a widespread phenomenon in the ocean. They are trains of short-period vertical displacements of water layers. They are described as trains of IS that propagate to the shelf coast. IIWs are caused by internal tides [20–22]. The parameters of IIWs are presented in Table 1 in accordance with the experimental data [18–22]. These parameters lead to specific acoustic phenomena due to IIWs. The study in [23] demonstrates that IIWs traveling across the acoustic path between the source and receiver significantly influence the horizontal refraction of acoustic rays propagating at small angles relative to the IIW wavefronts. Consequently, the resulting dynamic waveguides in the horizontal plane align nearly parallel to the IIW fronts. The impact of this acoustic phenomenon on the holographic structure generated by a moving source was examined in detail in our previous paper [51]. Conversely, IIWs propagating along the acoustic path between the source and receiver induce strong coupling between acoustic modes. This mode coupling results in a redistribution of sound energy across the modes, altering the balance of modal amplitudes within the sound field structure. The following sections of the paper analyze how these effects influence the process of source holographic reconstruction.

The "vertical modes and horizontal rays" approach shows that horizontal dynamic waveguides are selective for sound modes. The structure of horizontal rays differs for different sound modes. The structure of the horizontal rays of the sound modes also depends on frequency, as shown in [23]. The resonance-like form of this frequency dependence is evident in the propagation of broadband sound signals.

Table 1. Parameters of IIWs

Parameter	Value
Train length	$L \sim 3$–$5\,\mathrm{km}$
Count of internal solitons	$N \sim 4$–7
Traveling velocity	$u_n \sim 0.5$–$1\,\mathrm{m/s}$
Internal soliton amplitude	$B_n \sim 10$–$30\,\mathrm{m}$
Internal soliton width	$\eta_n \sim 100$–$200\,\mathrm{m}$
Interval between solitons	$D_n \sim 300$–$500\,\mathrm{m}$
Curvature radius of wave front	$R \sim 15$–$25\,\mathrm{km}$

3. Structure of the Source Interferogram due to IIWs

This section presents the model of the source interferogram in the presence of IIWs propagating along the acoustic path. It consists of three parts. The first part (Section 3.1) describes the sound field model in a waveguide with IIWs, using the vertical modes and horizontal rays approximation framework. Section 3.2 presents the mode coupling approach to account for the sound field due to inhomogeneities caused by IIWs. Section 3.3 considers the structure of the interferogram of a broadband source moving in a waveguide in the presence of IIWs.

3.1. Sound Field Model in a Waveguide with IIWs

Within the framework of the vertical modes and horizontal rays approximation, the complex acoustic field in a shallow waveguide influenced by IIWs, which is described by Eqs. (1)–(10), can be expressed as follows, cf. [23,38,51,52]:

$$p(\mathbf{r}, z, \omega, t) = \sum_{m=0}^{M} P_m(\mathbf{r}, \omega, t)\phi_m(z, \omega), \tag{11}$$

Here, $\mathbf{r} = (x, y)$ denotes the horizontal position vector of the source, P_m represents the amplitude of the m-th mode, and $\phi_m(z, \omega)$ denotes the vertical structure (mode shape) of the corresponding acoustic mode in a waveguide unaffected by IIWs. The complex horizontal wavenumber of each mode is given by $\bar{\xi}_m(\omega) = \bar{h}_m(\mathbf{r}, \omega, t) + \mathrm{i}\bar{\gamma}_m(\mathbf{r}, \omega, t)$, where $\bar{h}_m$ and $\bar{\gamma}_m$ are its real and imaginary parts, respectively. The summation extends to M, the total number of modes considered. As a result, the acoustic pressure field p depends on the angular frequency $\omega = 2\pi f$. The eigenfunctions $\phi_m(z, \omega)$ and the complex wavenumbers $\bar{\xi}_m$ are obtained by solving the associated Sturm–Liouville eigenvalue problem with boundary conditions corresponding to a free surface and a bottom, cf. [51,52]:

$$\frac{d^2\phi_m(\omega, z)}{dz^2} + k^2\bar{n}^2(z)\,\phi_m(\omega, z) = \bar{\xi}_m^2\phi_m(\omega, z), \tag{12}$$

$$\phi_m(\omega, z)\big|_{z=0} = 0, \quad \phi_m(\omega, z)\big|_{z=H} + g(\bar{\xi}_m)\frac{d\phi_m(\omega, z)}{dz}\Big|_{z=H} = 0, \tag{13}$$

where

$$g(\xi_m) = \eta \Big/ \sqrt{\bar{\xi}_m^2 - k^2 n_b^2 (1 + \mathrm{i}\varkappa)}. \tag{14}$$

The functions $\phi_m(\omega, z)$ are orthonormalized:

$$\int_0^H \phi_l \phi_m \, dz + \eta \int_H^\infty \phi_l \phi_m \, dz = \delta_{ml}, \tag{15}$$

where δ_{ml} is the Kronecker delta symbol.

3.2. Coupling Modes due to IIWs

Let us consider the coupled-mode approach [41–46,52] to take into account the scattering of the sound field Eq. (11) induced by the inhomogeneities of the water layer caused by IIWs. In the mode amplitude $P_m(\mathbf{r}, \omega, t)$, we isolate the factor corresponding to cylindrical spreading:

$$P_m(\mathbf{r}, \omega, t) = \frac{C_m(\mathbf{r}, \omega, t)}{\sqrt{\bar{h}_m r}}, \tag{16}$$

where $C_m(\mathbf{r}, \omega, t)$ denotes the mode amplitude without the cylindrical spreading factor, and $\bar{h}_m$ is the real part of the mode horizontal wavenumber. The horizontal range between source and receiver is r. This representation explicitly factors out the geometric spreading term $1/\sqrt{r}$, which dominates the range dependence in the shallow water waveguide under consideration.

Under the forward scattering approximation, the Helmholtz equation for the sound field reduces to a first-order system of ordinary differential equations that describes the evolution of coupled mode amplitudes $C_m(r, \omega, t)$:

$$\frac{dC_m(r, \omega, t)}{dr} = \mathrm{i} \sum_{l=1}^{M} \left(\bar{\xi}_m \delta_{ml} + \mu_{ml}(r, \omega, t) \right) C_l(r, \omega, t). \tag{17}$$

Here, the complex mode horizontal wavenumber is defined as $\bar{\xi}_m(\omega) = \bar{h}_m(\mathbf{r}, \omega, t) + \mathrm{i}\bar{\gamma}_m(\mathbf{r}, \omega, t)$. The mode coupling coefficients due to IIWs are $\mu_{ml}(r, \omega, t)$:

$$\mu_{ml}(r, \omega, t) = \frac{k^2}{2\sqrt{\bar{h}_m \bar{h}_l}} \int_0^H \phi_m(\omega, z) \, \tilde{n}^2(\mathbf{r}, z, t), \phi_l(\omega, z) \, dz. \tag{18}$$

Thus, the problem of simulating the sound field in an inhomogeneous, shallow water waveguide with IIWs can be reduced to determining the waveguide modes without IIWs (see Eqs. (12)–(15)) and solving the system of differential equations for the coupling mode amplitudes (see Eqs. (17)–(18)). This system of differential equations must be supplemented with an initial source condition. For a point omnidirectional source located at the coordinates $r = r_0$ and $z = z_0$, this condition takes the form: $C_m(0, \omega, t) = \phi_m(\omega, z_0)$, up to a constant factor.

The numerical solution of Eqs. (17)–(18) has the following matrix form:

$$\mathbf{C}(r + \Delta r, \omega, t) = \exp\{\mathrm{i}\,\mathbf{M}(r, \omega, t)\,\Delta r\}\mathbf{C}(r, \omega, t). \tag{19}$$

Here, $\mathbf{C}(r, \omega, t) = \{C_m(r, \omega, t)\}$ is the vector of the mode amplitudes, $\mathbf{C}(0) = \{C_m(0, \omega, t)\}$ is the vector of initial amplitude values, The matrix of mode coupling coefficients $\mathbf{M}(r, \omega, t)$ has following form:

$$\mathbf{M}(r, \omega, t) = \left\{ \bar{\xi}_m(r, \omega)\, \delta_{nm} + \mu_{nm}(r, \omega, t) \right\}. \tag{20}$$

3.3. Interferogram Structure of a Moving Source in the Presence of IIWs

In the "vertical modes and horizontal rays approximation" framework, Eq. (11), the interferogram $I(\omega, t)$ of the moving source in the frequency-time domain (ω, t) can be written as:

$$\begin{aligned} I(\omega,t) &= \sum_m \sum_n A_m(\omega,t)\, A_n^*(\omega,t) \exp\left[\mathrm{i}\bar{h}_{mn}(\omega)(x_0 - vt)\right] \\ &= \sum_m \sum_n I_{mn}(\omega,t), \quad m \neq n, \end{aligned} \tag{21}$$

where $\bar{h}_{mn}(\omega) = \bar{h}_m(\omega) - \bar{h}_n(\omega)$. Here, $I_{mn}(\omega, t)$ - partial interferogram due to interference of m-th and n-th modes, $A_m(\omega, t)$ - amplitude of the $m-$th acoustic mode ($A_m(\omega,t) = P_m(\omega,t)\phi_m(z,\omega)\exp(-\mathrm{i}\bar{h}_m r)$), x_0 - initial source coordinate at time $t_0 = 0$, t - current time, v - velocity of the moving source. The superscript "*" denotes the complex conjugate value. The condition $m \neq n$ means that the mean value has been removed from the interferogram $I(\omega, t)$.

4. Structure of the Source Hologram due to IIWs

In this section, we examine the holographic representation of a moving acoustic source in the presence of IIWs interactions. To extract holographic features, we apply a 2D-FT to the interferogram $I(\omega, t)$ from Eq. (21) in the joint frequency–time domain (ω, t). This yields the hologram $F(\tau, \widetilde{\nu})$ in the following form:

$$\begin{aligned} F(\tau,\widetilde{\nu}) &= \sum_m \sum_n \int_0^{\Delta t} \int_{\omega_1}^{\omega_2} I_{mn}(\omega,t)\, \exp\left[\mathrm{i}(\widetilde{\nu}t - \omega\tau)\right] dt\, d\omega \\ &= \sum_m \sum_n F_{mn}(\tau,\widetilde{\nu}), \end{aligned} \tag{22}$$

where τ is the time lag and $\widetilde{\nu} = 2\pi\nu$ is the angular frequency in the hologram domain. The quantity $F_{mn}(\tau, \widetilde{\nu})$ corresponds to the modal interference between the m-th and n-th acoustic modes. The frequency integration is performed over the range $\omega_1 = \omega_0 - \Delta\omega/2$ to $\omega_2 = \omega_0 + \Delta\omega/2$. Here, $\Delta\omega$ is the bandwidth of the signal, ω_0 is the central (reference) frequency, and Δt is the duration of the observation. To further simplify the analysis, we use a linearized approximation of modal dispersion:

$$\bar{h}_m(\omega) = \bar{h}_m(\omega_0) + \left.\frac{d\bar{h}_m}{d\omega}\right|_{\omega=\omega_0} (\omega - \omega_0). \tag{23}$$

Assuming that the frequency dependence of the modal amplitudes, P_m, and the spectral content of the sound field vary slowly compared to the rapid phase oscillations of the term $\exp[\mathrm{i}\, h_m(\omega)(x_0 + vt)]$, the expression for the partial hologram in Eq. (22) can be rewritten in a simplified form

$$\begin{aligned} F_{mn}(\tau,\widetilde{\nu}) = A_m(\omega_0)A_n^*(\omega_0)\Delta\omega\Delta t \exp[\mathrm{i}\Phi_{mn}(\tau,\widetilde{\nu})]\times \\ \times \frac{\sin\Big\{\big[x_0\frac{\mathrm{d}\bar{h}_{mn}(\omega_0)}{\mathrm{d}\omega} - \tau\big]\frac{\Delta\omega}{2}\Big\}\sin\Big\{\big[v\bar{h}_{mn}(\omega_0) + \widetilde{\nu}\big]\frac{\Delta t}{2}\Big\}}{\big[x_0\frac{\mathrm{d}\bar{h}_{mn}(\omega_0)}{\mathrm{d}\omega} - \tau\big]\frac{\Delta\omega}{2}\big[v\bar{h}_{mn}(\omega_0) + \widetilde{\nu}\big]\frac{\Delta t}{2}}, \end{aligned} \tag{24}$$

where $\Phi_{mn}(\tau, \widetilde{\nu})$ is the phase of the $F_{mn}(\tau, \widetilde{\nu})$ - partial hologram

$$\Phi_{mn}(\tau,\widetilde{\nu}) = \Big(\frac{\widetilde{\nu}\Delta t}{2} - \tau\omega_0\Big) + \bar{h}_{mn}(\omega_0)\Big(\frac{\Delta t}{2}v + x_0\Big). \tag{25}$$

It is important to note that Eq. (24) is derived under the assumption that $x_0 \gg v\Delta t$. In the $(\tau, \widetilde{\nu})$ domain, the hologram $F(\tau, \widetilde{\nu})$ is concentrated within two compact regions that appear as focal spots. These regions are positioned as follows:

1. I and III quadrants if the source moves toward the receiver ($v < 0$),

2. II and IV quadrants if the source moves away from the receiver ($v > 0$).

The distribution $F(\tau, \widetilde{\nu})$ contains $M - 1$ distinct focal spots, each of which is located at the coordinates $(\tau_\mu, \widetilde{\nu}_\mu)$ along a straight line defined by the equation $\widetilde{\nu} = \widetilde{\varepsilon}\tau$. The index $\mu = 1, 2, \ldots, M - 1$ enumerates the focal spots. Each spot at $(\tau_\mu, \widetilde{\nu}_\mu)$ represents a location where the maxima of $M - \mu$ partial holograms constructively interfere. The slope $\widetilde{\varepsilon} = 2\pi\varepsilon$ of this line can also be expressed as $\widetilde{\varepsilon} = -\delta\omega/\delta t$. Here, $\delta\omega$ is the shift in frequency corresponding to the peak of the interference pattern over the time interval δt.

The dimensions of each focal spot along the τ and $\widetilde{\nu}$ axes are identical for all spots and independent of their total count. These dimensions are given by:

$$\delta\tau = \frac{4\pi}{\delta\omega}, \quad \delta\widetilde{\nu} = \frac{4\pi}{\delta t}. \tag{26}$$

The initial distance and radial velocity of the source can be determined for the focal spot nearest to the origin of the hologram plane using the following expressions from [16]:

$$\dot{v} = -k_v \widetilde{\nu}_1, \qquad \dot{x}_0 = k_x \tau_1, \tag{27}$$

where

$$k_v = (M-1)\Big(h_{1M}(\omega_0)\Big)^{-1}, \qquad k_x = (M-1)\Big(\mathrm{d}h_{1M}(\omega_0)/\mathrm{d}\omega\Big)^{-1}. \tag{28}$$

Unlike the actual source parameters, the values estimated through processing are denoted with an overdot. The holographic signal processing technique is implemented as follows. During the total observation window Δt, the interferogram $I(\omega, t)$ is constructed by quasi-coherently summing J statistically independent realizations of the received signal. Each realization has a duration of t_1 and is separated from the others by a time gap of t_2. This is done over the frequency range of $\Delta\omega$. The number of realizations is given by:

$$J = \frac{\Delta t}{t_1 + t_2}. \tag{29}$$

To ensure statistical independence between realizations, the condition $t_2 > 2\pi/\Delta\omega$ must be satisfied. Then, the constructed interferogram $I(\omega, t)$ is transformed using 2D-FT, resulting in the hologram $F(\tau, \widetilde{\nu})$ corresponding to the moving source in the waveguide environment.

In general, the spatial-spectral structure of the hologram $F(\tau, \widetilde{\nu})$ differs significantly from that of the original interferogram $I(\omega, t)$. Nevertheless, a one-to-one correspondence exists between them: the hologram $F(\tau, \widetilde{\nu})$ uniquely represents the content of the interferogram $I(\omega, t)$. Thus, applying an inverse 2D-FT to $F(\tau, \widetilde{\nu})$ allows for the complete reconstruction of the initial interferogram $I(\omega, t)$.

5. Numerical Simulation Results

This section discusses the outcomes of numerical simulations concerning the interferogram $I(\omega, t)$ and the hologram $F(\tau, \widetilde{\nu})$ for a broadband acoustic source in a shallow water waveguide. The simulations account for intense internal waves (IIWs), which induce mode coupling. The simulation examines the effects of IIWs on the interferogram and hologram of the source's acoustic field under two different source configurations. The first scenario uses a fixed source-receiver geometry (i.e., a stationary source), and the second uses a dynamic configuration with a moving source. To enable meaningful comparisons of the effects of IIWs in both scenarios, the simulations use identical initial parameters.

Section 5 is divided into three subsections. Section 5.1 details the characteristics of the shallow water waveguide and the parameters of the acoustic source. Section 5.2 presents the modeling results for the stationary source case. Section 5.3 provides an analysis of the results for the moving source configuration.

5.1. Shallow Water Waveguide and Sound Field Parameters

The waveguide model used in the simulation is based on parameters representative of the SWARM'95 experiment, conducted off the coast of New Jersey in 1995 [18,19]. In the numerical calculations, the sound speed profile $c(z)$ is adopted according to observational data collected in the experimental area between 18:00–20:00 GMT on August 4, 1995 [18].

Numerical modeling is carried out for the acoustic parameters of a shallow water waveguide (see Table 2). Two frequency bands are considered: $\Delta f_1 = 100 - 120\,\text{Hz}$ and $\Delta f_2 = 300 - 320\,\text{Hz}$. For the first frequency band Δf_1, the bottom refractive index is: $n_b = 0.84\,(1 + \mathrm{i}\,0.03)$, bottom density: $\rho_b = 1.8\,\text{g/cm}^3$, and modes count: $M = 4$. For the second frequency band Δf_2, the bottom refractive index is $n_b = 0.84\,(1 + \mathrm{i}\,0.05)$, the bottom density is $\rho_b = 1.8\,\text{g/cm}^3$, and the modes count is $M = 10$. The initial range is $x_0 = 10\,\text{km}$ between the source and the receiver. The depth of the source is $z_s = 12.5\,\text{m}$. The depth of the receiver is $z_q = 35\,\text{m}$. The source spectrum is uniform. Sound pulses are recorded periodically at an interval of 5 s. The sampling frequency is 0.25 Hz. The observation time is $T = 20\,\text{min}$.

Table 2. Acoustic parameters of shallow water waveguide

Parameter	$\Delta f_1 = 100$–120 **Hz**	$\Delta f_2 = 300$–320 **Hz**
Bottom refractive index	$n_b = 0.84\,(1 + \mathrm{i}\,0.03)$	$n_b = 0.84\,(1 + \mathrm{i}\,0.05)$
Bottom density	$\rho_b = 1.8\,\text{g/cm}^3$	$\rho_b = 1.8\,\text{g/cm}^3$
Modes count	$M = 4$	$M = 10$

In the first frequency band $\Delta f_1 = 100$–$120\,\text{Hz}$, the sound field consists of $M = 4$ propagating modes. The parameters of the sound field mode, $h_m(\omega_0)$ and their frequency derivatives $\frac{dh_m(\omega_0)}{d\omega}$, are presented in Table 3. As can be seen, $h_m(\omega_0) \sim 0.43 - 0.46$ m $^{-1}$ and $\frac{dh_m(\omega_0)}{d\omega} \sim 6.7 \cdot 10^4 - 7.1 \cdot 10^4$ $(\text{m/s})^{-1}$.

Table 3. Sound field mode parameters ($\Delta f_1 = 100$–$120\,\text{Hz}$)

m**-th mode**	h_m**, m**$^{-1}$	$(dh_m/d\omega) \cdot 10^4$**, (m/s)**$^{-1}$
1	0.4635	6.762
2	0.4557	6.808
3	0.4450	6.901
4	0.4310	7.091

In the second frequency band, $\Delta f_2 = 300$–$320\,\text{Hz}$, the sound field consists of $M = 10$ propagating modes. The parameters of the sound field mode, $h_m(\omega_0)$ and their frequency derivatives $\frac{dh_m(\omega_0)}{d\omega}$, are presented in Table 4. As can be seen in Table 4, $h_m(\omega_0) \sim 1.2 - 1.3$ m $^{-1}$ and $\frac{dh_m(\omega_0)}{d\omega} \sim 6.7 \cdot 10^4 - 7.1 \cdot 10^4$ $(\text{m/s})^{-1}$.

Table 4. Sound field mode parameters ($\Delta f_2 = 300$–$320\,\text{Hz}$)

m**-th mode**	h_m**, m**$^{-1}$	$(dh_m/d\omega) \cdot 10^4$**, (m/s)**$^{-1}$
1	1.312	6.751
2	1.307	6.761
3	1.300	6.781
4	1.292	6.797
5	1.282	6.808
6	1.273	6.815
7	1.263	6.831
8	1.252	6.875
9	1.240	6.970
10	1.225	7.057

The geometries of the numerical simulations are shown in Figures 1 and 2. IIWs travel along the acoustic path connecting the source and receiver. The internal soliton parameters are presented in Table 5. The amplitude is $B_n = 15\,\mathrm{m}$, the width is 150 m, velocity: $u_n = 0.7\,\mathrm{m/s}$. The wavefront is plane ($R = \infty$).

Table 5. Internal soliton parameters

Parameter	Value
Amplitude	$B_n = 15\,\mathrm{m}$
Width	$\eta_n = 150\,\mathrm{m}$
Velocity	$u_n = 0.7\,\mathrm{m/s}$
Wavefront	$R = \infty$

5.2. Results of Numerical Simulation. First Case: Non-Moving Source ($v = 0$ m/s)

Consider the results of the numerical model for the first case, which is a non-moving source ($v = 0\,\mathrm{m/s}$). The source-receiver range is $x_0 = 10\,\mathrm{km}$. The source depth is $z_s = 12.5\,\mathrm{m}$. The receiver depth is $z_q = 35\,\mathrm{m}$. The source spectrum is uniform. The sound pulses are recorded periodically at an interval of 5 s. The sampling frequency is 0.25 Hz. The observation time is $T = 20\,\mathrm{min}$. We consider the two frequency bands $\Delta f_1 = 100 - 120\,\mathrm{Hz}$ (Table 1) and $\Delta f_2 = 300 - 320\,\mathrm{Hz}$ (Table 2).

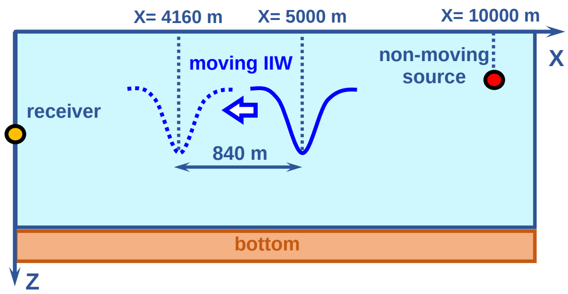

Figure 3. Numerical simulation model. IIWs is traveling along the acoustic path ($u = 0.7\,\mathrm{m/s}$). First case: non-moving source ($v = 0\,\mathrm{m/s}$).

The numerical simulation model is shown in Figure 3. It is assumed that the intense internal waves (IIW) are traveling along the acoustic path with a velocity of $u_n = 0.7\,\mathrm{m/s}$ from the source to the receiver. The IIWs are displaced by $\Delta x = 840\,\mathrm{m}$ during the $T = 20\,\mathrm{min}$ observation period. The initial position of the IIWs is $x = 5000\,\mathrm{m}$. The final position of the IIWs is $x = 4160\,\mathrm{m}$.

The outcomes of the numerical simulations are presented in Figures 4–10. Figures 4 and 5 illustrate the interferogram $I(f,t)$ and the corresponding hologram $F(\tau, \widetilde{\nu})$ in the absence of IIWs. Figure 4 represents the frequency band $\Delta f_1 = 100$–$120\,\mathrm{Hz}$, while Figure 5 refers to the frequency band $\Delta f_2 = 300$–$320\,\mathrm{Hz}$. The interferogram $I(f,t)$ is characterized by vertical, spatially localized fringes. The holographic representation $F(\tau, \widetilde{\nu})$ features focal points aligned along the horizontal axis, which is typical for a stationary (non-moving) sound source. As the frequency increases, both the structural complexity of $I(f,t)$ and the number of focal points in $F(\tau, \widetilde{\nu})$ grow. This effect is due to the greater number of propagating acoustic modes at higher frequencies (see Tables 3 and 4).

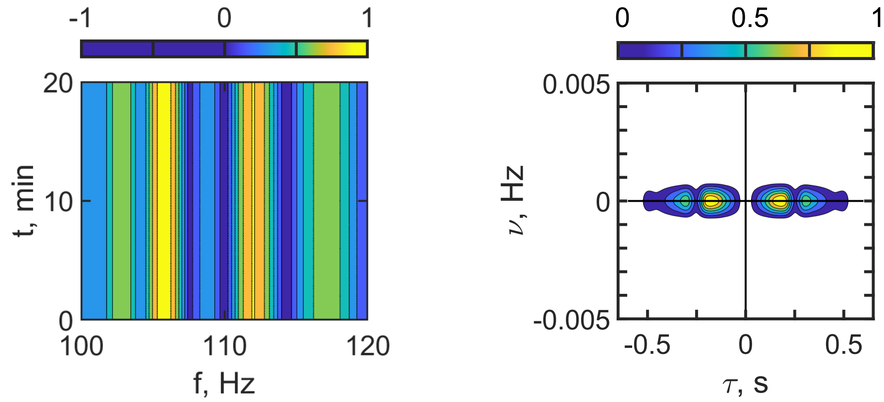

(**a**) (**b**)

Figure 4. Interferogram $I(f,t)$ (**a**). Hologram $F(\tau,\widetilde{\nu})$ (**b**). Frequency band: $\Delta f_1 = 100 - 120\,\text{Hz}$. Non-moving source: $v = 0\,\text{m/s}$. IIWs are absent.

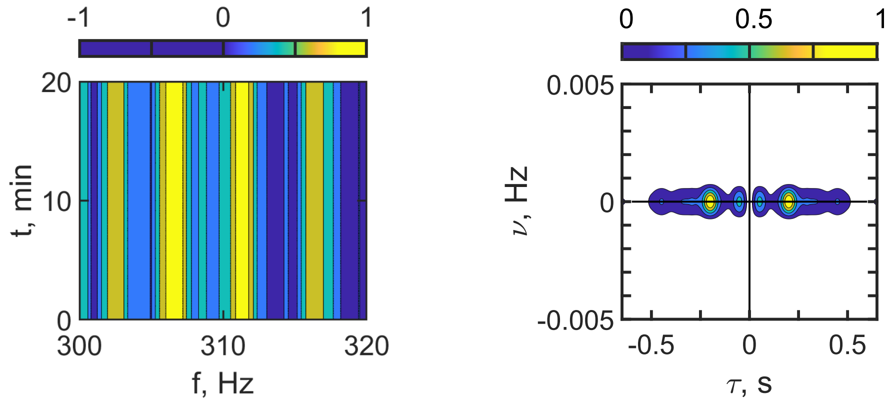

(**a**) (**b**)

Figure 5. Interferogram $I(f,t)$ (**a**). Hologram $F(\tau,\widetilde{\nu})$ (**b**). Frequency band: $\Delta f_2 = 300 - 320\,\text{Hz}$. Non-moving source: $v = 0\,\text{m/s}$. IIWs are absent.

Figures 6 and 7 show the interferogram $I(f,t)$ and the hologram $F(\tau,\widetilde{\nu})$ in the presence of IIWs. It is assumed that the IIWs travel along the acoustic path from the source to the receiver. Figure 6 corresponds to the frequency band $\Delta f_1 = 100$–$120\,\text{Hz}$, and Figure 7 to $\Delta f_2 = 300$–$320\,\text{Hz}$. In the lower frequency range $\Delta f_1 = 100$–$120\,\text{Hz}$, where mode coupling due to IIWs is weak, the resulting interferogram is dominated by vertically localized fringes (Figure 6(a)), which are characteristic of a shallow water waveguide in the absence of IIWs. As the frequency increases to $\Delta f_2 = 300$–$320\,\text{Hz}$, the effects of mode coupling caused by IIWs become more pronounced. The contribution of mode coupling to the sound field intensifies, resulting in the formation of horizontally localized fringes (Figure 7(a)). Consequently, the structure of the interferogram $I(f,t)$ becomes more complex.

Two types of focal spots appear in the hologram domain (see Figures 6(b), 7(b)). The focal spots that correspond to the vertical fringes of the interferogram $I(f,t)$, i.e., the shallow water waveguide without IIWs, are concentrated along the time axis τ. The focal spots that correspond to the horizontal fringes, i.e., the result of mode coupling due to IIWs, are concentrated along the frequency axis $\widetilde{\nu}$. Outside of these focal spots, the spectral density is almost completely suppressed. Under natural conditions, an internal wave train (IIWT) consists of multiple internal solitons with varying parameters, which leads to a blurring of the distinct structure in both the interferogram $I(f,t)$ and the hologram $F(\tau,\widetilde{\nu})$. The arrangement of focal spots in the hologram $F(\tau,\widetilde{\nu})$ makes it possible to separate the component corresponding to the undisturbed waveguide from the component of the sound field that is perturbed by IIWs.

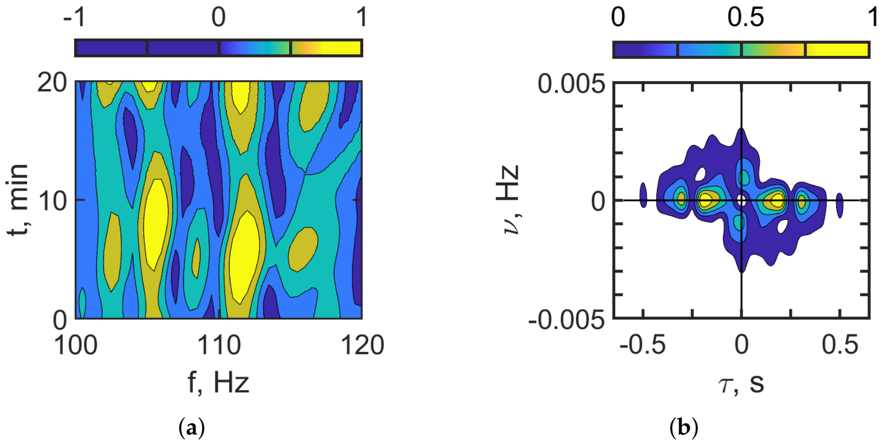

Figure 6. Interferogram $I(f,t)$ (**a**). Hologram $F(\tau,\widetilde{\nu})$ (**b**). Frequency band: $\Delta f_1 = 100 - 120\,\text{Hz}$. Non-moving source: $v = 0\,\text{m/s}$. IIWs are present ($B_n = 15\,\text{m}$, $u_n = 0.7\,\text{m/s}$).

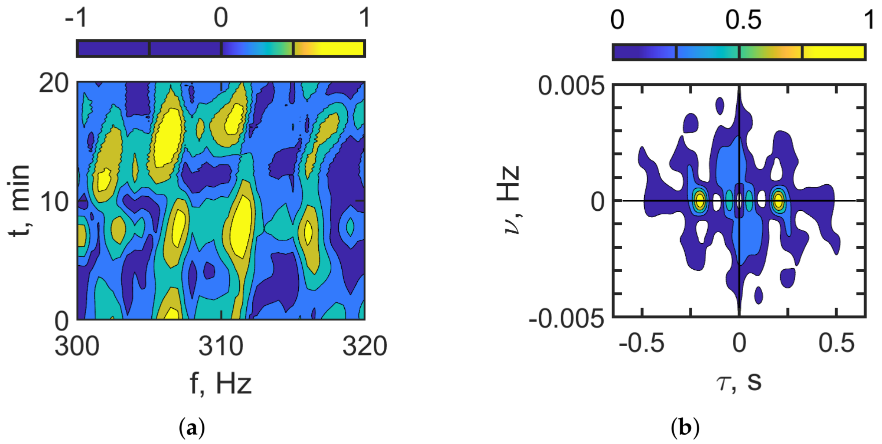

Figure 7. Interferogram $I(f,t)$ (**a**). Hologram $F(\tau,\widetilde{\nu})$ (**b**). Frequency band: $\Delta f_2 = 300 - 320\,\text{Hz}$. Non-moving source: $v = 0\,\text{m/s}$. IIWs are present ($B_n = 15\,\text{m}$, $u_n = 0.7\,\text{m/s}$).

Figures 8 and 9 present the results of applying a filter to the hologram to isolate the focal spots aligned horizontally in Figures 6 and 7, followed by an inverse 2D Fourier transform (2D-FT) to obtain the corresponding interferograms. These interferograms and holograms (Figures 8 and 9) closely resemble those representing the undisturbed waveguide scenario (without IIWs), as shown in Figures 4 and 5. A comparison reveals that the positions and structures of the focal spots remain consistent between the original and reconstructed holograms. Figure 10 provides further evidence by comparing one-dimensional slices of the two-dimensional interferograms $I(f,t)$ at a fixed time $t_0 = 0\,\text{min}$. The red curve represents the case without IIWs, and the blue curve represents the case with IIWs, highlighting the similarity and confirming the effectiveness of the separation method.

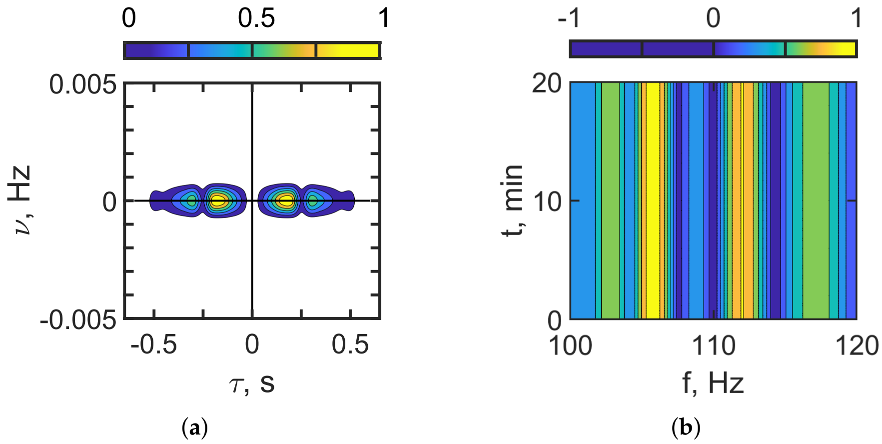

Figure 8. Filtered hologram $F(\tau,\widetilde{\nu})$ (**a**). Filtered interferogram $I(f,t)$ (**b**). Frequency band: $\Delta f_1 = 100 - 120\,\mathrm{Hz}$. Non-moving source: $v = 0\,\mathrm{m/s}$. IIWs are present ($B_n = 15\,\mathrm{m}$, $u_n = 0.7\,\mathrm{m/s}$).

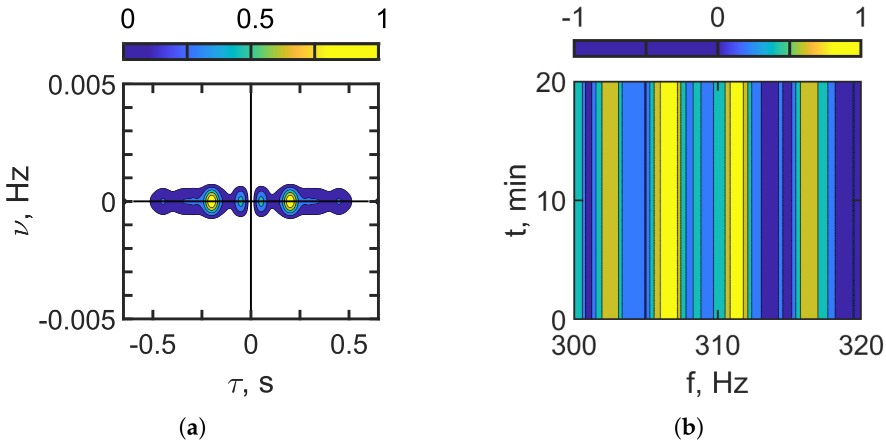

Figure 9. Filtered hologram $F(\tau,\widetilde{\nu})$ (**a**). Filtered interferogram $I(f,t)$ (**b**). Frequency band: $\Delta f_2 = 300 - 320\,\mathrm{Hz}$. Non-moving source: $v = 0\,\mathrm{m/s}$. IIWs are present ($B_n = 15\,\mathrm{m}$, $u_n = 0.7\,\mathrm{m/s}$).

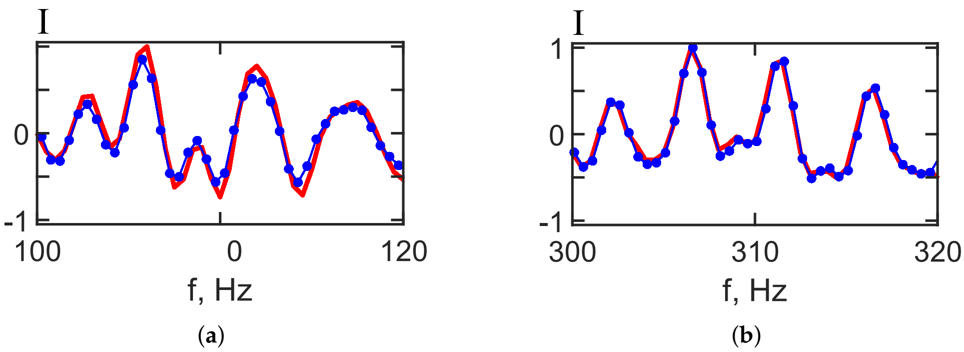

Figure 10. Interferogram $I(f,t)$ slice ($t_0 = 0\,\mathrm{min}$) reconstructed by holographic filtering: (**a**) frequency band - $\Delta f_1 = 100 - 120\,\mathrm{Hz}$ and (**b**) frequency band - $\Delta f_2 = 300 - 320\,\mathrm{Hz}$. Non-moving source: $v = 0\,\mathrm{m/s}$. Red curve - IIWs are absent. Blue curve - IIWs are present ($B_n = 15\,\mathrm{m}$, $u_n = 0.7\,\mathrm{m/s}$).

The interferogram reconstruction error is estimated using the dimensionless quantity:

$$d = \frac{\sum_{j=1}^{J} |I_1(f_j) - I_2(f_j)|}{\sum_{j=1}^{J} |I_1(f_j)|}, \tag{30}$$

where $I_1(f)$ and $I_2(f)$ are the initial and reconstructed 1D-interferograms, respectively. The interferogram reconstruction error values for the frequency bands $\Delta f_1 = 100 - 120$ Hz and $\Delta f_2 = 300 - 320$ Hz are presented in Table 6.

Table 6. Interferogram reconstruction error values

No.	$\Delta f_1 = 100$–120 **Hz**	$\Delta f_2 = 300$–320 **Hz**
1.	$d_1 = 0.014$	$d_2 = 0.074$
2.	$J = 80$	$J = 80$

The numerical modeling outcomes for the frequency band $\Delta f_2 = 300$–320 Hz are consistent with those obtained for the lower frequency range $\Delta f_1 = 100$–120 Hz. These results demonstrate that the proposed approach can separate the sound field into two components: one associated with the undisturbed waveguide and one resulting from the influence of IIWs. Consequently, it is possible to reconstruct the interferogram of the unperturbed waveguide even when the source is stationary and IIWs are present.

5.3. Results of Numerical Simulation. Second Case: Moving Source ($v = 1$ m/s)

Consider the results of the numerical model for the second case, which involves a moving source ($v = 1$ m/s). Initially, at $t_0 = 0$ min, the distance between the source and the receiver is set to $x_0 = 10$ km. The source is positioned at a depth of $z_s = 12.5$ m, and the receiver is located at $z_q = 35$ m. A uniform spectrum is assumed for the acoustic source. Each emitted sound pulse has a duration of $t_1 = 4$ s, with a sampling frequency of 0.25 Hz. The interval between consecutive pulses is $t^* = 5$ s, which includes a $t_2 = 1$ s pause after each pulse ($t^* = t_1 + t_2$). The total observation time is $\Delta T = 20$ min. Two frequency ranges are analyzed: $\Delta f_1 = 100$–120 Hz (Table 1) and $\Delta f_2 = 300$–320 Hz (Table 2).

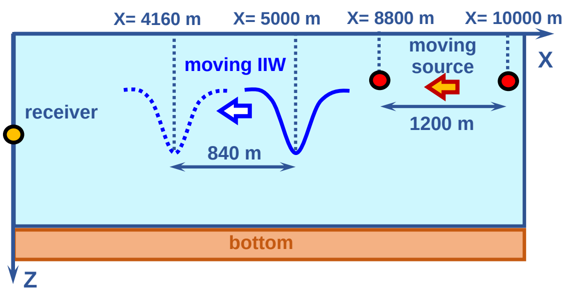

Figure 11. Numerical simulation model. IIW travels along the acoustic path ($u = 0.7$ m/s). Second case: moving source ($v = 1$ m/s).

The numerical simulation model is illustrated in Figures 11. It is assumed that IIWs propagate along the acoustic path from the source to the receiver at a velocity of $u_n = 0.7$ m/s. During the observation period of $T = 20$ min, the IIWs travel a distance of $\Delta x = 840$ m. Their initial position is $x = 5000$ m, and by the end of the observation period, they reach $x = 4160$ m. During the same 20-minute interval, the acoustic source moves horizontally along the x-axis toward the receiver at a constant speed of $v = 1$ m/s, covering a distance of $\Delta x = 1200$ m. The source's initial location is $x = 10000$ m, and its final position is $x = 8800$ m.

Figures 12 and 13 present the interferogram $I(f,t)$ and the corresponding hologram $F(\tau, \widetilde{\nu})$ for a moving source in the absence of intense internal waves (IIWs). Figure 12 illustrates the case for the frequency band $\Delta f_1 = 100$–120 Hz, Figure 13 refers to the frequency band $\Delta f_2 = 300$–320 Hz. The interferograms $I(f,t)$ are characterized by localized, slanted fringes. In the hologram domain, $F(\tau, \widetilde{\nu})$, the energy is concentrated in a series of focal spots in the I and III quadrants. As the frequency increases, both the complexity of the interferogram and the number of focal spots in the hologram grow, similar to the behavior observed with a non-moving source.

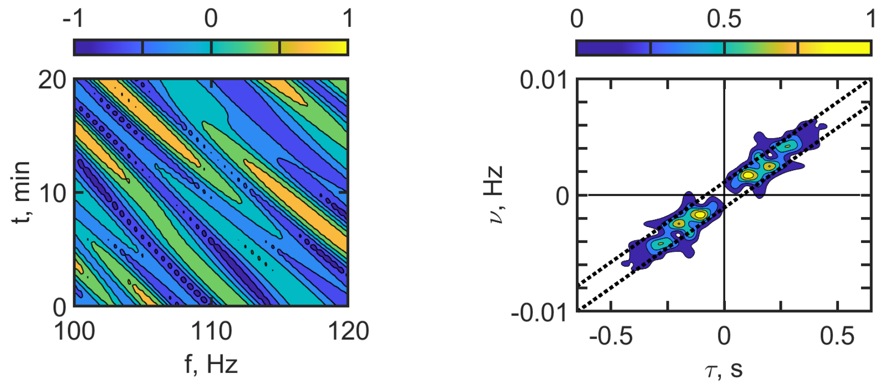

(**a**) (**b**)

Figure 12. Interferogram $I(f,t)$ (**a**). Hologram $F(\tau,\widetilde{\nu})$ (**b**). Frequency band: $\Delta f_1 = 100 - 120\,\mathrm{Hz}$. Moving source: $v = 1\,\mathrm{m/s}$. IIWs are absent.

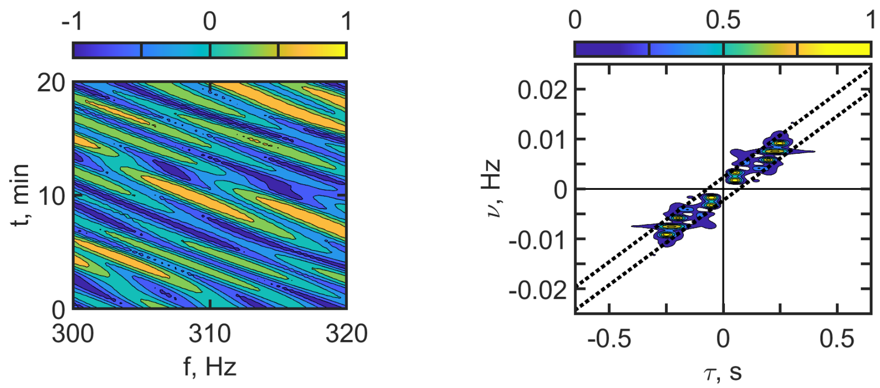

(**a**) (**b**)

Figure 13. Interferogram $I(f,t)$ (**a**). Hologram $F(\tau,\widetilde{\nu})$ (**b**). Frequency band: $\Delta f_2 = 300 - 320\,\mathrm{Hz}$. Moving source: $v = 1\,\mathrm{m/s}$. IIWs are absent.

In the hologram domains in Figures 12 (b) and 13 (b) dashed lines are shown. These dashed lines indicate the region where the focal spots of the sound field in shallow water without IIWs are concentrated. The linear dimensions of this region are approximately: $\delta\tau \approx 0.15\,\mathrm{s}$, $\delta\nu \approx 0.002\,\mathrm{Hz}$, which agrees with the theoretical focal spot dimension estimates, Eq. (26): $\delta\tau = 0.1\,\mathrm{s}$, $\delta\nu = 0.0017\,\mathrm{Hz}$. The interferogram and hologram parameters for the case of a moving source and the absence of IIWs are presented in Table 7 for the frequency bands: $\Delta f_1 = 100$–$120\,\mathrm{Hz}$ and $\Delta f_2 = 300$–$320\,\mathrm{Hz}$.

Table 7. Interferogram and hologram structure parameters. Estimation of source parameters.

No.	$\Delta f_1 = 100$–120 **Hz**	$\Delta f_2 = 300$–320 **Hz**
1.	$\delta f/\delta t \approx -0.016\,\mathrm{s}^{-2}$	$\delta f/\delta t \approx -0.035\,\mathrm{s}^{-2}$
2.	$\tau_1 = 1.0 \cdot 10^{-1}\,\mathrm{s}$	$\tau_1 = 3.8 \cdot 10^{-1}\,\mathrm{s}$
3.	$\nu_1 = 1.71 \cdot 10^{-3}\,\mathrm{Hz}$	$\nu_1 = 2.0 \cdot 10^{-3}\,\mathrm{Hz}$
4.	$\dot{v} = 0.99\,\mathrm{m/s}$	$\dot{v} = 1.3\,\mathrm{m/s}$
5.	$\dot{x}_0 = 9.1\,\mathrm{km}$	$\dot{x}_0 = 11.1\,\mathrm{km}$

Figures 14 and 15 show the interferogram $I(f,t)$ and the hologram $F(\tau,\widetilde{\nu})$ of the moving source in the case of IIWs traveling along the acoustic path between the source and the receiver. Figure 14 corresponds to $\Delta f_1 = 100 - 120\,\mathrm{Hz}$ and Figure 15 corresponds to $\Delta f_2 = 300 - 320\,\mathrm{Hz}$. Significant mode coupling due to IIWs leads to distortions of interferograms fringes $I(f,t)$ and the appearance of additional intense focal spots in the holograms $F(\tau,\widetilde{\nu})$ compared to the shallow water waveguide without IIWs. The sound intensity along the interferogram fringes becomes highly nonuniform, taking the form of focal spots, as shown in Figures 14(a) and 15(a). This effect becomes more pronounced with an increasing frequency band. This is explained by the strengthening of the mode coupling effects due to the IIWs as the frequency increases. In the hologram domain, Figures 14(b) and 15(b), the concentration of focal spots along the frequency axis ν increases with the increase in the frequency band. This indicates the dominant influence of IIWs on the hologram structure.

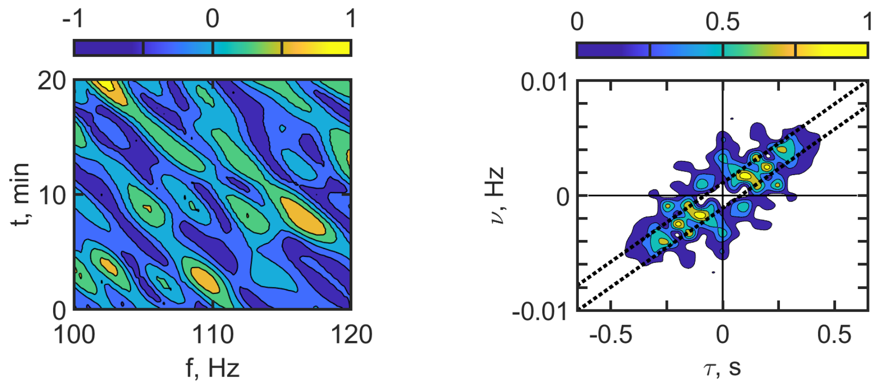

(**a**) (**b**)

Figure 14. Interferogram $I(f,t)$ (**a**). Hologram $F(\tau,\widetilde{\nu})$ (**b**). Frequency band: $\Delta f_1 = 100 - 120\,\mathrm{Hz}$. Moving source: $v = 1\,\mathrm{m/s}$. IIWs are present ($B_n = 15\,\mathrm{m},\ u_n = 0.7\,\mathrm{m/s}$).

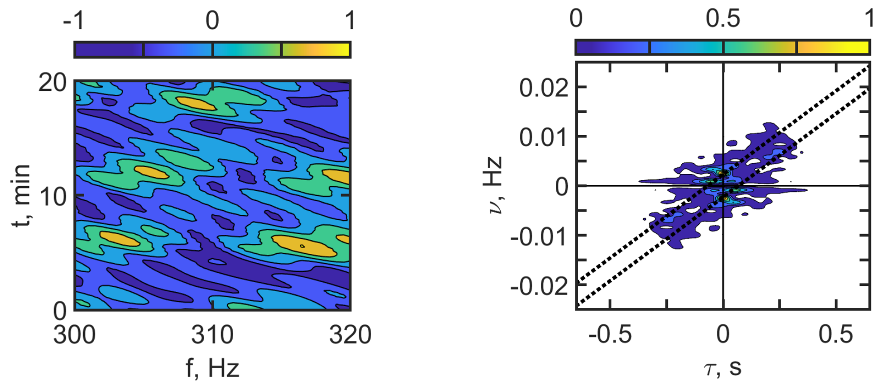

(**a**) (**b**)

Figure 15. Interferogram $I(f,t)$ (**a**). Hologram $F(\tau,\widetilde{\nu})$ (**b**). Frequency band: $\Delta f_2 = 300 - 320\,\mathrm{Hz}$. Moving source: $v = 1\,\mathrm{m/s}$. IIWs are present ($B_n = 15\,\mathrm{m}$, $u_n = 0.7\,\mathrm{m/s}$).

The spatial distribution of focal spots in the hologram $F(\tau,\widetilde{\nu})$ for a moving source allows one to distinguish between the component of the acoustic field component associated with an undisturbed waveguide and the component influenced by IIWs. Figures 14 and 15 display the results of applying a filter to the focal spots located along the dotted lines in the holograms. The corresponding interferograms, obtained via inverse 2D-FT, are shown in Figures 16 and 17. The reconstructed interferograms and holograms in these figures closely resemble those in Figuress 12 and 13, which show the case without IIWs. A comparison reveals that the positions of the focal spots in both the original and reconstructed holograms are nearly identical. The interferogram and hologram parameters for the case of a moving source and the presence of IIWs are presented in Table 8 for the frequency bands $\Delta f_1 = 100$–$120\,\mathrm{Hz}$ and $\Delta f_2 = 300$–$320\,\mathrm{Hz}$.

Table 8. Interferogram and hologram structure parameters. Estimation of source parameters.

No.	$\Delta f_1 = 100$–$120\,$**Hz**	$\Delta f_2 = 300$–$320\,$**Hz**
1.	$\delta f/\delta t \approx -0.016\,\mathrm{s}^{-2}$	$\delta f/\delta t \approx -0.035\,\mathrm{s}^{-2}$
2.	$\tau_1 = 1.19 \cdot 10^{-1}\,\mathrm{s}$	$\tau_1 = 4.08 \cdot 10^{-1}\,\mathrm{s}$
3.	$\nu_1 = 2.00 \cdot 10^{-3}\,\mathrm{Hz}$	$\nu_1 = 1.63 \cdot 10^{-3}\,\mathrm{Hz}$
4.	$\dot{v} = 1.1\,\mathrm{m/s}$	$\dot{v} = 1.1\,\mathrm{m/s}$
5.	$\dot{x}_0 = 10.8\,\mathrm{km}$	$\dot{x}_0 = 12.0\,\mathrm{km}$

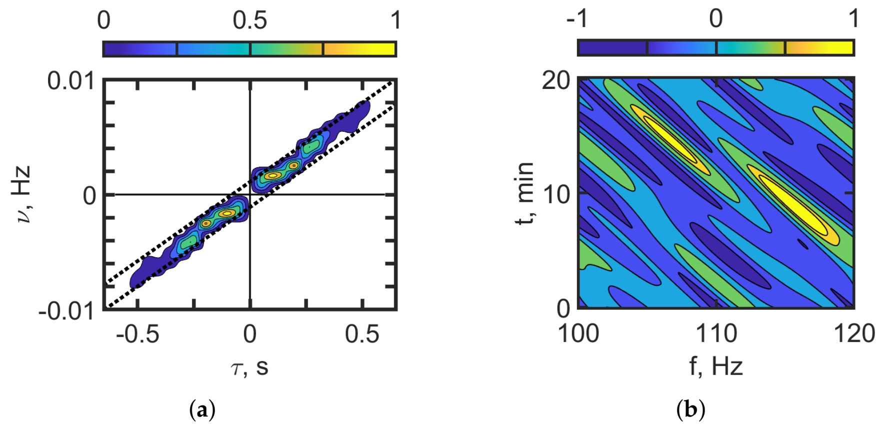

Figure 16. Filtered hologram $F(\tau, \tilde{\nu})$ (**b**). Filtered interferogram $I(f, t)$ (**a**). Frequency band: $\Delta f_1 = 100 - 120\,\mathrm{Hz}$. Moving source: $v = 1\,\mathrm{m/s}$. IIWs are present ($B_n = 15\,\mathrm{m}$, $u_n = 0.7\,\mathrm{m/s}$).

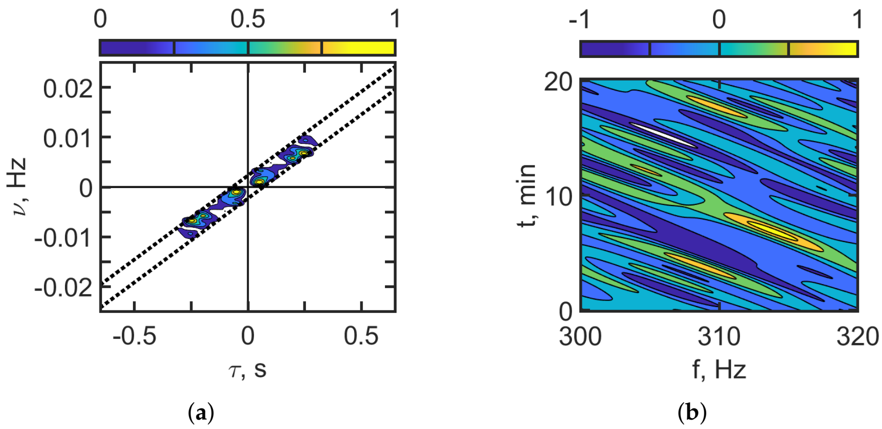

Figure 17. Filtered hologram $F(\tau, \tilde{\nu})$ (**b**). Filtered interferogram $I(f, t)$ (**a**). Frequency band: $\Delta f_2 = 300 - 320\,\mathrm{Hz}$. Moving source: $v = 1\,\mathrm{m/s}$. IIWs are present ($B_n = 15\,\mathrm{m}$, $u_n = 0.7\,\mathrm{m/s}$).

As can be seen, the focal spots on the reconstructed and initial holograms of the moving source are the same. Figure 18 shows the proximity of the initial and reconstructed interferograms of the moving source. Figure 18 shows the 1D interferograms for $t_0 = 0\,\mathrm{min}$. The red curve shows that IIWs are not present. The blue curve shows that IIWs are present. The interferogram reconstruction error values (Eq. (30)) for the frequency bands $\Delta f_1 = 100 - 120\,\mathrm{Hz}$ and $\Delta f_2 = 300 - 320\,\mathrm{Hz}$ are presented in Table 9.

Table 9. Interferogram reconstruction error values

No.	$\Delta f_1 = 100$–$120\,$**Hz**	$\Delta f_2 = 300$–$320\,$**Hz**
1.	$d_1 = 0.635$	$d_2 = 0.821$
2.	$J = 80$	$J = 80$

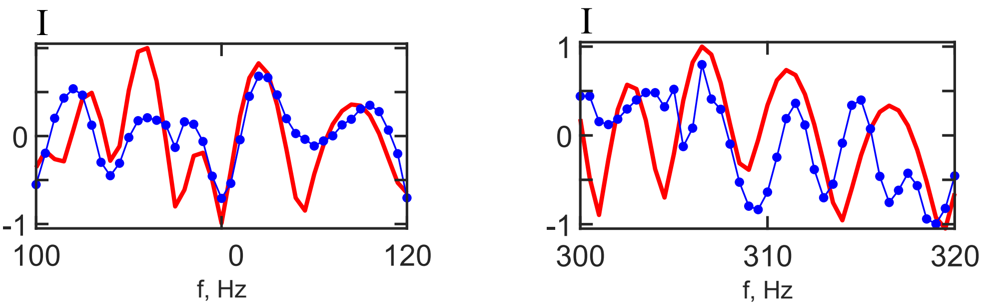

(**a**) (**b**)

Figure 18. Reconstructed 1D-interferogram $I(f)$ (**a**) $\Delta f_1 = 100 - 120\,\text{Hz}$ and (**b**) $\Delta f_2 = 300 - 320\,\text{Hz}$. Moving source: $v = 1\,\text{m/s}$. Red curve - IIWs are absent. Blue curve - IIWs are present.

Compared to the stationary source scenario, the reconstruction error for the frequency bands $\Delta f_1 = 100$–$120\,\text{Hz}$ and $\Delta f_2 = 300$–$320\,\text{Hz}$ increases by factors of 45.4 and 11.1, respectively. This suggests that reconstructing the interferogram of a waveguide without IIWs is less accurate when the source is in motion. The observed difference in error magnitudes arises from the varying nature of propagation conditions. While a stationary source is solely affected by variability introduced by IIWs, a moving source experiences additional variability due to its own motion, which compounds the effects of IIW-induced mode coupling.

6. Conclusions

We examined the robustness of the holographic signal processing (HSP) method in the presence of intense internal waves (IIWs) for a moving broadband acoustic source. It is assumed that the IIWs travel along the acoustic path between the source and the receiver. Under these conditions, the IIWs cause significant scattering of sound intensity and mode coupling. The stability of the HSP method depends on the structural characteristics of the hologram produced by the moving source in the presence of IIWs. This hologram consists of two components. The first corresponds to the sound field propagating through an unperturbed shallow water waveguide (i.e., without IIWs), and the second represents the waveguide perturbation caused by IIW-induced mode coupling.

This separation of the hologram's structure allows for the isolation of individual components of the acoustic field. The component associated with the unperturbed waveguide can be extracted with minimal distortion. This isolated component of the hologram is then used to reconstruct the interferogram of the moving source in a shallow water waveguide without IIWs.

Although the reconstructed interferograms differ from the original ones mainly in terms of contrast when IIWs are present, the angular slopes of the interference fringes remain unchanged. Therefore, it is still feasible to estimate key source parameters, such as range, velocity, and direction, based on the reconstructed unperturbed component of the sound field, even in the presence of IIWs. Furthermore, the accuracy of these estimations increases with operating frequency.

Author Contributions: Supervision and project administration, M.E. and S.P.; conceptualization and methodology, V.K. and S.P.; software, S.T., A.P., and N.L.; validation, M.E. and V.K.; formal analysis, M.E. and S.P.; writing – original draft preparation, M.E. and S.P.; writing – review and editing, M.E. and S.P.; All authors have read and agreed to the published version of the manuscript.

Funding: This work was supported by grant from the Russian Science Foundation № 23-61-10024, https://rscf.ru/project/23-61-10024/.

Data Availability Statement: The original data used in the study are openly available. The waveguide model used in the simulation is based on parameters from the SWARM'95 experiment, [18,19].

Conflicts of Interest: The authors declare no conflicts of interest.

Abbreviations

The following abbreviations are used in this manuscript:

HSP	holographic signal processing;
ISP	interferometric signal processing;
3DHE	3D Helmholtz Equation models;
3DPE	3D Parabolic Equation models;
3DR	3D Ray-based models;
VMMPE	Vertical Modes and 2D Modal Parabolic Equation models;
VCMHR	Vertical Coupled Modes with Horizontal Rays models;
IIW	intense internal wave;
IS	internal soliton;
KdV	Korteweg-de Vries;
2D	two-dimensional;
3D	three-dimensional;
1D-FT	one-dimensional Fourier transform;
2D-FT	two-dimensional Fourier transform.

References

1. Weston D, Stevens K. Interference of wide-band sound in shallow water. *J. Sound Vib. 21(1):57–64.* **1972**.
2. Chuprov S. Interference structure of a sound field in a layered ocean. *Ocean Acoust., Curr. State. 71–91.* **1982**.
3. Ianniello J. Recent developments in sonar signal processing. *IEEE Signal Proc. Magazine, 15(4):27-40.* **1998**.
4. Thode AM. Source ranging with minimal environmental information using a virtual receiver and waveguide invariant theory. *J. Acoust. Soc. Am., 108(4):1582-1594.* **2000**.
5. Kuperman WA, D'Spain GL. Ocean acoustic interference phenomena and signal processing. *Ocean Acoust. Interfer. Phenom. Signal Proc. 621.* **2002**.
6. Rouseff D, Spindel RC. Modeling the waveguide invariant as a distribution. *AIP Conf. Proc., Amer. Inst. Phys. 621:137-150.* **2002**.
7. Baggeroer AB. Estimation of the distribution of the interference invariant with seismic streamers. *AIP Conf. Proc., Amer. Inst. Phys. 621:151-170.* **2002**.
8. Yang T. Beam intensity striations and applications. *J. Acoust. Soc. Am., 113(3):1342-1352.* **2003**.
9. Heaney KD. Rapid geoacoustic characterization using a surface ship of opportunity. *IEEE J. Oceanic Engrg., 29(1):88-99.* **2004**.
10. Cockrell KL, Schmidt H. Robust passive range estimation using the waveguide invariant. *J. Acoust. Soc. Am., 127(5):2780-2789.* **2010**.
11. Rouseff D, Zurk LM. Striation-based beam forming for estimating the waveguide invariant with passive sonar. *J. Acoust. Soc. Am. Express Lett., 130:76–81.* **2011**.
12. Harrison CH. The relation between the waveguide invariant, multipath impulse response, and ray cycles. *J. Acoust. Soc. Am., 129(5):2863-2877.* **2011**.
13. Emmetiere R, Bonnel J, Gehant M, Cristol X, Chonavel Th. Understanding deep-water striation patterns and predicting the waveguide invariant as a distribution depending on range and depth. *J. Acoust. Soc. Am., 143(6):3444-3454.* **2018**.
14. Emmetiere R, Bonnel J, Cristol X, Gehant M, Chonavel T. Passive source depth discrimination in deep-water. *IEEE J. Select. Topics Signal Process., 13(1):185-197.* **2019**.
15. Kuznetsov GN, Kuzkin VM, Pereselkov SA. Spectrogram and localization of a sound source in a shallow sea. *Acoust. Phys., 63(4):449-461.* **2017**.
16. Ehrhardt M, Pereselkov SA, Kuz'kin VM, Kaznacheev I, Rybyanets P. Experimental observation and theoretical analysis of the low-frequency source interferogram and hologram in shallow water. *J. Sound Vibr. 544:117388.* **2023**.
17. Kuz'kin VM, Pereselkov SA, Zvyagin VG, Malykhin AYu, Prosovetskiy DYu. Intense internal waves and their manifestation in interference patters of received signals on oceanic shelf. *Phys. Wave Phenom., 26(2):160-167.* **2018**.
18. Badiey M and SWARM'95 group. Cruise Report. Ocean Acoustic Experiments in Support of Shallow Water Acoustic Remote Measurements (SWARM). *University of Delaware P. 72.* **1995**.

19. Apel JR, Badiey M, Chiu C-S, Finette S, Headrick RH, Kemp J, Lynch JF, Newhall AE, Orr MH, Pasewark BH, Tielburger D, Turgut A, von der Heydt K, Wolf SN. An overview of the SWARM 1995 shallow-water internal wave acoustic scattering experiment. *IEEE J. Ocean. Engrg., 22:465-500.* **1997**.
20. Serebryany AN. Manifestation of the properties of solitons in internal waves on the shelf. *Izv. Acad. Sci. USSR, Phys. Atmosphere Ocean, 29(2):285-293.* **1993**.
21. Ostrovsky LA, Stepanyants YuA. Do internal solitons exist in the ocean? *Reviews of Geophysics 27:293-310.* **1989**.
22. Konyaev KV, Sabinin KD. Waves inside the ocean. *St. Petersburg, Gidromet. Publ., 271 p.* **1992**.
23. Katsnelson BG, Pereselkov SA. Low-frequency horizontal acoustic refraction caused by internal wave solitons in a shallow sea. *Acoust. Phys., 46(6):684-691.* **2000**.
24. Pereselkov S, Kuz'kin V, Ehrhardt M, Tkachenko S, Rybyanets P, Ladykin, N. Three-Dimensional Modeling of Sound Field Holograms of a Moving Source in the Presence of Internal Waves Causing Horizontal Refraction. *J. Mar. Sci. Eng. 11, 1922.* **2023**
25. Lin Y-T, Porter MB, Sturm F, Isakson MJ, Chiu C-S. Introduction to the special issue on three-dimensional underwater acoustics. *J. Acoust. Soc. Am., 146(3):1855–1857.* **2019**.
26. Liu W, Zhang L, Wang W, Wang Y, Ma S, Cheng X, Xiao W. A three-dimensional finite difference model for ocean acoustic propagation and benchmarking for topographic effects. *J. Acoust. Soc. Am., 150(2):1140–1156.* **2021**.
27. Tu H, Wang Y, Liu W, Yang C, Qin J, Ma S, Wang X. Application of a Spectral Method to Simulate Quasi-Three-Dimensional Underwater Acoustic Fields. *J. Sound Vibr., 545:117421.* **2023**.
28. Larsson E, Abrahamsson L. Helmholtz and parabolic equation solutions to a benchmark problem in ocean acoustics. *J. Acoust. Soc. Am., 113(5):2446–2454.* **2003**.
29. Smith KB, Tappert FD. UMPE: The University of Miami Parabolic Equation Model. *Version 1.1 "MPL Technical Memorandum 432", P. 96.* **1993**.
30. Tappert FD. The parabolic approximation method. Lecture Notes in Physics, V. 70, Eds. J.B. Keller, J.S. Papadakis, Eds., Wave Propagation and Underwater Acoustics, *Springer-Verlag, New York, Chapter 5, pp. 224-287.* **1977**.
31. Lin Y-T. Three-dimensional boundary fitted parabolic-equation model of underwater sound propagation. *J. Acoust. Soc. Am., 146(3):2058–2067.* **2019**.
32. Heaney KD, Campbell RL. Three-dimensional parabolic equation modeling of mesoscale eddy deflection. *J. Acoust. Soc. Am., 139(2):918–926.* **2016**.
33. Ivansson S. Local accuracy of cross-term corrections of three-dimensional parabolic-equation models. *J. Acoust. Soc. Am., 146(3):2030–2040.* **2019**.
34. Lee K, Seong W, Na Y. Three-dimensional Cartesian parabolic equation model with higher-order cross-terms using operator splitting, rational filtering, and split-step Padé algorithm. *J. Acoust. Soc. Am., 146(3):2030–2040.* **2019**.
35. Lee K, Seong W, Na Y. Split-step Padé solver for three dimensional Cartesian acoustic parabolic equation in stair-step representation of ocean environment. *J. Acoust. Soc. Am., 146(3):2050–2057.* **2019**.
36. Porter MB. Beam tracing for two- and three-dimensional problems in ocean acoustics. *J. Acoust. Soc. Amer., 146(3):2016–2029.* **2019**.
37. Porter MB. Bellhop3d User Guide. *La Jolla, CA: Heat, Light, and Sound Research, Inc.* **2016**.
38. Collins MD. The adiabatic mode parabolic equation. *J. Acoust. Soc. Am. 94:2269–2278.* **1993**.
39. Trofimov MY, Kozitskiy S, Zakharenko A. A mode parabolic equation method in the case of the resonant mode interaction. *Wave Motion, 58:42–52.* **2015**.
40. Petrov PS, Sturm F. An explicit analytical solution for sound propagation in a three-dimensional penetrable wedge with small apex angle. *J. Acoust. Soc. Amer., 139(3):1343–1352.* **2016**.
41. Kohler W, Papanicolaou GC. Wave propagation in a randomly inhomogeneous ocean. In: Keller JB Papadakis JS (Eds.), Wave Propagation and Underwater Acoustics *Lecture Notes in Physics, Springer, 70:153–223.* **1977**.
42. Dozier LB, Tappert FD. Mode coupling – surface roughness. *J. Acoust. Soc. Amer., 63(2):353–365.* **1978**.
43. Dozier LB, Tappert FD. Mode coupling – bottom roughness. *J. Acoust. Soc. Amer., 63(2):365–370.* **1978**.
44. Fawcett JA. Coupled-mode equation refinements. *J. Acoust. Soc. Amer., 91(4):2052–2061.* **1992**.
45. Trofimov AS, et al. Formal derivations of mode coupling equations. *J. Mar. Sci. Eng., 11(4):797–812.* **2023**.
46. Colosi JA, Flatté SM. Mode coupling by internal waves. *J. Acoust. Soc. Amer., 100(6):3607–3620.* **1996**.
47. Preisig JC, Duda TF. Coupled acoustic mode propagation through continental-shelf internal solitary waves. *IEEE J. Oceanic Eng., 22(3):256–269.* **1997**.

48. Feng L, Goff JA, Yang B. Nonlinear internal-wave interaction. *J. Acoust. Soc. Amer., 116(4):2300–2310.* **2004**.
49. Colosi JA. Acoustic mode coupling induced by shallow water nonlinear internal waves: sensitivity to environmental conditions and space–time scales of internal waves. *J. Acoust. Soc. Amer., 124(3):1452–1464.* **2008**.
50. Yang TC. Acoustic mode coupling induced by nonlinear internal waves: evaluation of the mode coupling matrices and applications. *J. Acoust. Soc. Amer., 135(2):610–625.* **2014**.
51. Brekhovskikh LM, Lysanov YP. Fundamentals of Ocean Acoustics. *Springer.* **2013**.
52. Jensen FB, Kuperman WA, Porter MB, Schmidt H, Tolstoy A. Computational Ocean Acoustics. *Springer.* **2011**.